

33 **1 Introduction**

34 The Miocene (~23 to 5.3 Ma) marks a pivotal stage in Earth's long-term Cenozoic cooling trajectory, characterized
35 by major reorganization of the cryosphere, monsoon systems and global climate (Steinthorsdottir et al., 2021). The
36 warmest interval of this epoch, the Miocene Climatic Optimum (MCO, ~17–14 Ma), was marked by globally
37 elevated temperatures, reduced meridional temperature gradients, limited Antarctic sea ice, and intensified
38 hydrological activity in the tropics and subtropics (Holbourn et al., 2013; Steinthorsdottir et al., 2021). Following the
39 MCO, the climate transitioned toward cooler conditions, accompanied by stepwise expansion of Antarctic sea ice
40 and intensified monsoons circulation (e.g., (Steinthorsdottir et al., 2021; Holbourn et al., 2013; Holbourn et al.,
41 2018; Westerhold et al., 2020). These large-scale reorganizations have been widely interpreted as responses to
42 changes in external forcing acting on an evolving climate background state.

43 A growing body of evidence links these Miocene climate changes to orbital forcing, through mechanisms involving
44 Antarctic ice-sheet dynamics (Levy et al., 2019; Naish et al., 2009) and eccentricity-paced variations in the marine
45 carbon cycle associated with an intensified tropical hydrological cycle (Holbourn et al., 2007; Liu et al., 2024; Tian
46 et al., 2013). Long-term marine records further indicate that the sensitivity of Antarctic ice sheets to obliquity
47 forcing intensified from the Miocene onward and persisted into the Pliocene and Pleistocene (Levy et al., 2019; Van
48 Peer et al., 2024). Spectral analyses of benthic $\delta^{18}\text{O}$ and $\delta^{13}\text{C}$ records show dominant 400 kyr eccentricity pacing
49 during the Miocene, followed by the emergence of stronger 100 kyr and 40 kyr variability later in the Neogene
50 (Holbourn et al., 2007; Tian et al., 2013; Westerhold et al., 2020; Liu et al., 2024).

51 Orbital variation in eccentricity, obliquity, and precession regulate the seasonal and latitudinal distribution of
52 incoming solar radiation, thereby influencing the climate system such as monsoon strength, cryosphere dynamics,
53 and ocean–atmosphere coupling (Berger, 1978; Hays et al., 1976; Milanković, 1941). Specifically, summer
54 insolation in the high latitudes of the Northern Hemisphere (NH) has been suggested as a key driver of Quaternary
55 glacial-interglacial cycle (Milanković, 1941). Elevated NH summer insolation enhances land-sea thermal contrast,
56 shifts convection inland, strengthens rainfall from Africa to Southeast Asia (Battisti et al., 2014; Bosmans et al., 2018;
57 Dai et al., 2024; Herold et al., 2012; Yin et al., 2012). In the Southern Hemisphere, orbital forcing modulates
58 Antarctic ice-sheet sensitivity, with geological records indicating enhanced obliquity responses from the Miocene
59 onwards (Levy et al., 2019; Naish et al., 2009; Van Peer et al., 2024). Eccentricity-paced variations in the marine
60 carbon cycle and tropical hydrological processes further point to a strong imprint of long-period orbital forcing
61 during this interval (Holbourn et al., 2007; Tian et al., 2013; Liu et al., 2024).

62 However, the climate expression of orbital forcing is not stationary through time. Miocene $\delta^{18}\text{O}$ and $\delta^{13}\text{C}$ records are
63 dominated by 400 kyr eccentricity variability, whereas stronger 100 kyr and 40 kyr cycles emerge later in the
64 Neogene (Holbourn et al., 2007; Westerhold et al., 2020). Comparable shifts during the Mid-Pleistocene transition
65 (MPT) and the Mid-Brunhes Transition (MBT) occurred without major changes in orbital parameters, suggesting an
66 important role for background climate state, threshold behavior, or internal feedbacks related to the Southern Ocean
67 ventilation and Antarctic ice dynamics (Kemp et al., 2010; Yin, 2013). Recent analyses further emphasize changes

68 in the relative influence of precession and obliquity across these transitions (Berger et al., 2024). Collectively, these
69 observations imply a state-dependent orbital–climate relationship rather than a simple linear response to insolation
70 forcing.

71 Although geological archives document pervasive orbital pacing during the Miocene, the mechanisms by which
72 orbital-scale insolation variations translate into regional climate responses—particularly in warm climates lacking
73 large Northern Hemisphere ice sheets—remain poorly constrained. Proxy records alone cannot isolate the respective
74 roles of forcing, feedbacks, and internal variability, and climate modeling studies explicitly targeting orbital effects
75 under realistic Miocene boundary conditions remain scarce.

76 Here, we use fully coupled climate model simulations to evaluate the climate response to orbital-driven insolation
77 changes in the Miocene framework. We assess the sensitivity of high-latitude climate, tropical hydrological cycle,
78 and ocean-cryosphere interactions to orbital forcing, and how these responses differ from those under the pre-
79 industrial (PI) condition. By comparing these responses with those patterns inferred from proxy records, we assess
80 how background climate state modulates orbital-scale climate variability and to provide context for evaluation of
81 orbital-climate coupling through the Neogene.

82 **2 Climate model and simulation setup**

83 **2.1 FGOALS-g3 climate model and simulation setup**

84 We use the fully coupled general circulation model FGOALS-g3, which is part of CMIP6. It has been widely
85 applied to both present-day climate studies (Li et al., 2020; Lin et al., 2022; Wang et al., 2020) and paleoclimate
86 simulations from the Miocene to the mid-Holocene (Wei et al., 2023; Zheng et al., 2020). A detailed description of
87 model components and evaluation is provided in the Supplement.

88 Two baseline experiments were conducted: a pre-industrial (PI) simulation and a Miocene simulation (MCO). The
89 PI simulation is performed with standard pre-industrial climate forcing. The MCO simulation adopts the MioMIP2
90 protocol and incorporates reconstructed Miocene boundary conditions, including paleogeography, vegetation, ice
91 sheet, and an atmospheric CO₂ concentration three times the PI level (Burls et al., 2021). The solar constant, orbital
92 parameters, and aerosol concentration in MCO are kept identical to those of the PI simulation.

93 To examine the climate response to orbital forcing, we conducted sensitivity simulations by modifying orbital
94 parameters in each baseline experiment. For both the PI and MCO climate, we performed a “winter-perihelion”
95 simulation with minimum boreal summer insolation (NSI_{min}), and a “summer-perihelion” simulation with
96 maximum boreal summer insolation (NSI_{max}) (Table 1). These orbital simulations are designed to represent mid- to
97 late Miocene intervals characterized by pronounced δ¹³C excursions and widespread carbon burial associated with
98 the Monterey events (Anttila et al., 2023; Holbourn et al., 2018; Westerhold et al., 2020). Specifically, we selected
99 two representative time slices at 10.777 Ma (NSI_{max}) and 10.767 Ma (NSI_{min}) (Fig. S1). This orbital sensitivity
100 framework has been widely applied in previous Pleistocene studies (Battisti et al., 2014; Bosmans et al., 2018; Dai

101 et al., 2024). Although eccentricity also differs between these configurations, its effect is included in the effect of
 102 precession which amplitude is modulated by eccentricity.

103 **Table 1.** Model simulation setup

104

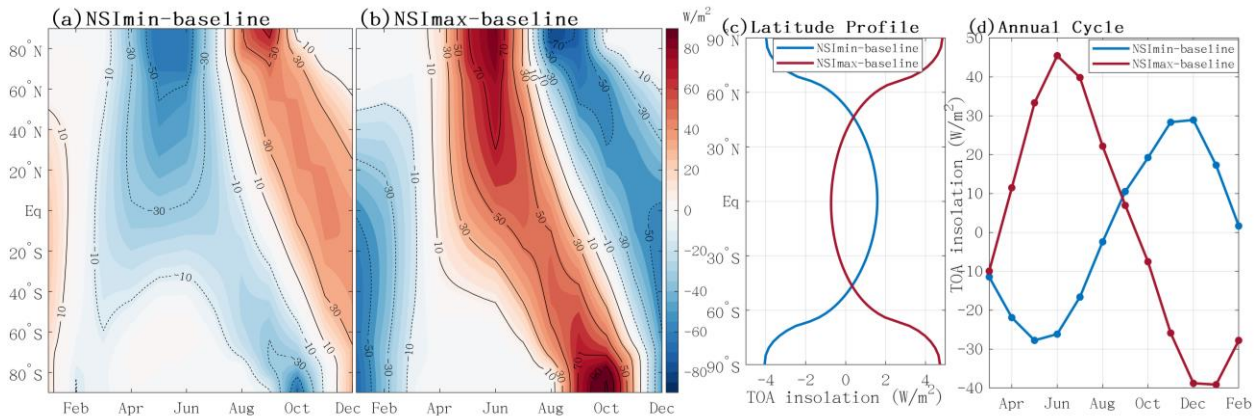
105

TOA*: Top-of-Atmosphere (TOA) radiation imbalance; GMAT**: Global Mean Air Temperature.

Simulation	Geography Setting	pCO ₂ (ppm)	Orbital forcing			Duration of simulation (yrs)	TOA* (W/m ²)	GMAT** (°C)
			Eccentr	Obliquity (rad)	Long. Perih			
PI			0.0167	0.4091	102.040°	1700	-0.04	15.61
PINSImax	Modern	280	0.0508	0.4208	281.387°	300	0.05	15.75
PINSImin			0.0599	0.3983	68.158°	300	-0.17	15.71
MCO			0.0167	0.4091	102.040°	1700	0.34	22.32
MCONSImax	Miocene	840	0.0508	0.4208	281.387°	400	0.28	22.47
MCONSImin	(~15Ma)		0.0599	0.3983	68.158°	400	0.30	22.58
MCO_1x		280	0.0167	0.4091	102.040°	1000	0.15	22.58

106

107 The June insolation contrast between NSImax and NSImin is substantial, reaching 130 W/m² at 65°N and 90 W/m²
 108 at 20°N (Fig. 1, S1 & S2). These seasonal insolation anomalies primarily result from differences in the longitude of
 109 perihelion (281° and 68°), corresponding to boreal summer and winter occurring near perihelion, respectively (Fig.
 110 S1 & Table 1). In NSImax, enhanced boreal summer insolation and reduced winter insolation amplify the globally
 111 averaged annual insolation cycle by ~80 W/m² relative to the baseline, whereas NSImin weakens the annual cycle
 112 by 60 W/m² (Fig. 1d). Meridionally, NSImax increases annual-mean insolation at high latitudes while slightly
 113 reducing it in the tropics due to its higher obliquity, with the opposite pattern in NSImin (Fig. 1c). Applying these
 114 orbital forcings yields two pairs of experiments: PINSImax/PINSImin for the pre-industrial and
 115 MCONSImax/MCONSIminAI for the Miocene. It's worth to note that although these specific configurations are
 116 chosen for the Miocene, similar orbital patterns recur throughout the Pleistocene (Fig. S3).



117

118 **Figure 1. Orbital-induced insolation changes (W/m^2) of the NSImin (a) and NSImax (b) simulations from the baseline**
119 **simulation, and their latitude profile of annual-mean insolation (c) and globally averaged annual insolation cycle (d).**

120 Both PI and MCO baseline simulations were each run for 1700 years to reach quasi-equilibrium. Orbital simulations
121 were then branched from the year 1601th of the corresponding baseline runs and integrated for additional 300
122 (PINSImax, PINSImin) and 400 years (MCONSImax, MCONSImin), respectively. Over the final 100 years of each
123 experiment, the global mean top-of-Atmosphere (TOA) radiation imbalance within $\pm 0.34 \text{ W/m}^2$ (Table. 1). Monthly
124 means from these equilibrated periods are used for all subsequent analysis. The PI simulation reasonably captures
125 the spatial pattern and magnitude of present-day seasonal temperature variations relative to the CMIP5 multi-model
126 mean and ERA5, with a minor cold bias in Arctic Eurasia linked to excessive sea ice (see SI for more details).

127 **2.2 Diagnostic analysis**

128 To diagnose the processes controlling the temperature response to orbital forcing, we apply a one-dimensional
129 Energy Balance Model analysis (EBM) following Heinemann et al. (2009) and Wei et al. (2023). The EBM
130 balances net incoming shortwave radiation against outgoing longwave radiation and meridional heat transport, using
131 radiative fluxes from the coupled general circulation model (GCM) as input. Temperature differences between
132 simulations are decomposed into contributions from surface albedo, water-vapor greenhouse trapping, cloud
133 radiative effects, and meridional heat transport. Cloud effects are further decomposed into shortwave and longwave
134 components.

135 The EBM components reproduce the zonal-mean temperature responses simulated by the GCM, with deviations
136 generally within $0.1\text{-}0.9 \text{ }^\circ\text{C}$ (Fig. S4). Slight underestimates occur in the NH subtropics and polar regions, while
137 overestimation appears near $70\text{-}80 \text{ }^\circ\text{N}$ (Fig. S4), consistent with previous studies and mainly reflecting nonlinear
138 processes associated with seasonal and zonal averaging (Lunt et al., 2012). The EBM decomposition is used to
139 interpret the relative roles of albedo, water vapour, clouds, and heat transport in shaping the spatial structure of
140 orbital-scale temperature changes.

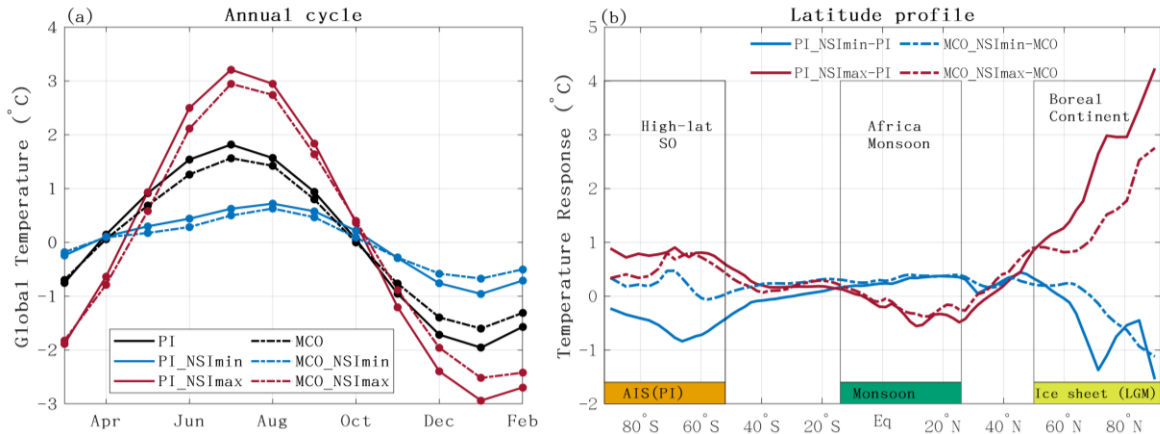
141 **3 Results and Discussion**

142 **3.1 Weaker seasonality of temperature response during the Miocene**

143 The annual temperature cycle in the MCO is $3.2 \text{ }^\circ\text{C}$, smaller than the $3.7 \text{ }^\circ\text{C}$ in PI, reflecting reduced July warming and
144 weaker January cooling (Fig 2a). The MCO-1x simulation shows an intermediate amplitude of $\sim 3.5 \text{ }^\circ\text{C}$ (Fig. S5),
145 suggesting both elevated CO_2 and Miocene boundary conditions contribute to the reduced seasonality, with the latter
146 exerting a slightly larger influence.

147 Orbital forcing substantially modulates the amplitude of the seasonal temperature cycle. Reduced boreal summer
148 insolation weakens the seasonal cycle by 1.9 to $1.3 \text{ }^\circ\text{C}$ in MCONSImin, and by $2.$ to $1.6 \text{ }^\circ\text{C}$ in PI_NSImin. Conversely,
149 increased boreal summer insolation intensifies seasonality, raising it to $5.4 \text{ }^\circ\text{C}$ in MCONSImax and $6.4 \text{ }^\circ\text{C}$ in
150 PI_NSImax (Fig. 2). Consequently, seasonal global-mean air temperature (GMAT) variations rise by more than $2 \text{ }^\circ\text{C}$

151 in the NSImax simulations and decline by a similar magnitude in the NSImin simulations relative to their respective
 152 baselines. The JJA temperature differences between NSImax and NSImin exceed 2.5 °C (Fig. 2), comparable to the
 153 ~3 °C global cooling during the late Miocene (Westerhold et al., 2020), underscoring the potential of orbital forcing
 154 to generate large-amplitude temperature variability.



155

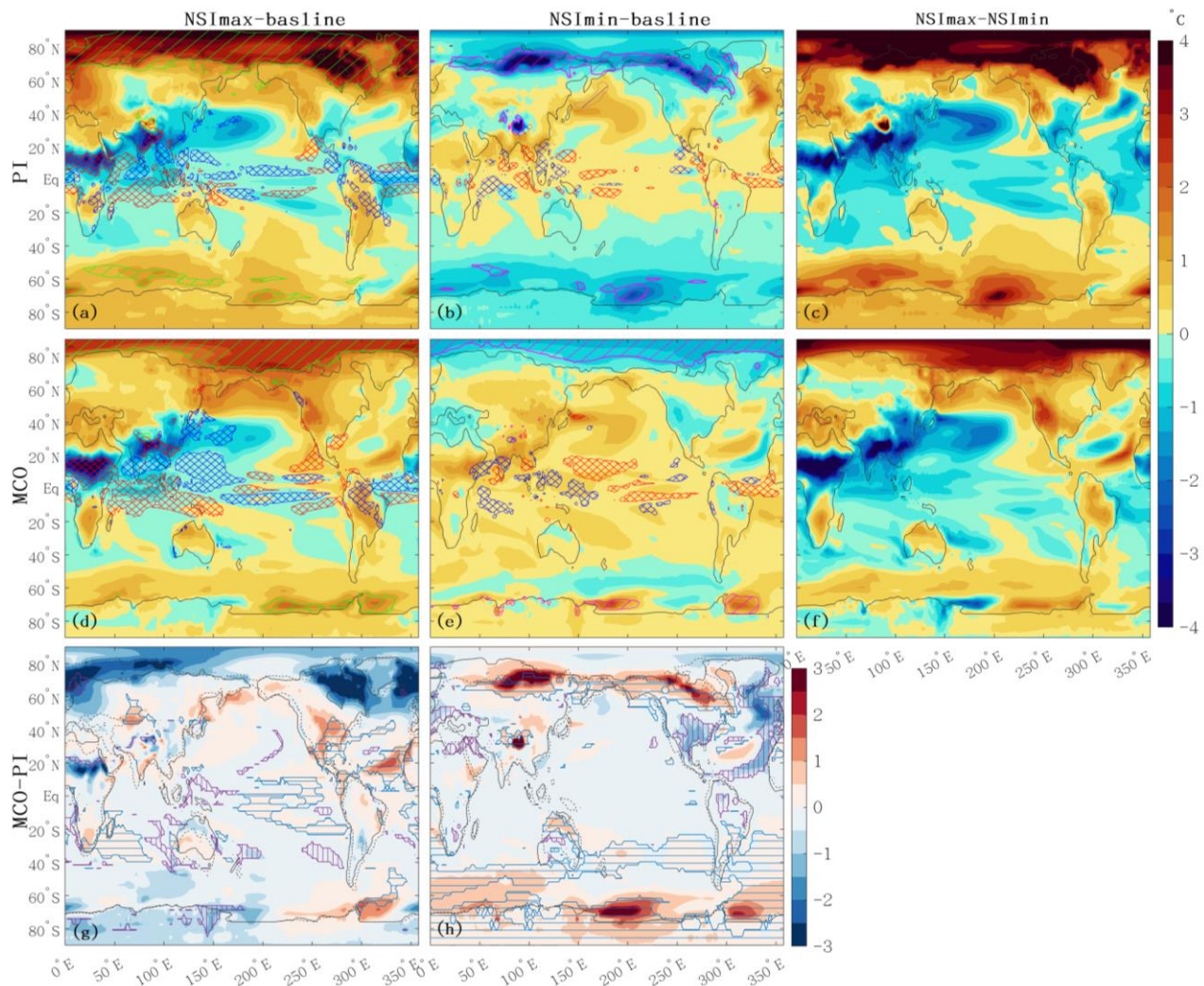
156 **Figure 2. (a) Annual cycle of temperature anomalies relative to the annual mean, with black, red and blue lines**
 157 **representing baseline, NSImax and NSImin simulations, respectively. Solid lines denote the PI climate, and dashed lines**
 158 **denote the Miocene climate. (b) Latitude profile of temperature response to orbital forcing, shown as anomalies to their**
 159 **baseline simulation and using the same color scheme as in (a). The locations of modern Antarctic Ice sheet (AIS), major**
 160 **monsoon regions and the Last glacial maximum Ice sheets are indicated in (b).**

161 Compared with the PI climate, the MCO simulation exhibits weaker seasonality and a dampened orbital response
 162 (Fig. 2a). The GMAT response to orbital forcing is diminished by ~ 0.1 °C in both MCONSImin and MCONSImax
 163 simulations, yielding ~10 % weaker changes in seasonal amplitude. This diminished Miocene temperature response
 164 is also evident in the latitudinal profile, showing differences of up to 1 °C at high latitudes (Fig. 2b). Because
 165 comparable analyses are not yet available for other warm climate intervals, it remains uncertain whether the
 166 reduced orbital response identified here is specific to the MCO or reflect a more general feature of warm climate
 167 states. This question requires further investigation.

168 This reduced Miocene seasonality is consistent with proxy-based evidence for weaker seasonality during the
 169 warming Miocene in Europe (Harzhauser et al., 2011), the Mediterranean (Utescher et al., 2009), and N.America
 170 (Reichgelt et al., 2023). Variation in Miocene seasonal response to identical orbital forcing can alter the relationship
 171 between growing-season and annual mean temperatures, potentially biasing proxy-based temperature
 172 reconstructions. This highlight the importance of applying seasonality adjustments that account for different
 173 paleoclimate background, rather than relying solely on modern analogues, when addressing well-documented
 174 seasonal biases in proxies (Bova et al., 2021; Marsicek et al., 2018; Laepple and Lohmann, 2009; Laepple et al.,
 175 2022).

176 **3.2 Spatially varied Miocene temperature responses**

177 The NSImax and NSImin simulations show overall anti-phased annual mean temperature responses (Fig. 3).
 178 Compared to the MCO and PI baselines, NSImax simulations show a dipole pattern, with polar warming but cooling
 179 in the tropics and subtropics of both hemispheres. Conversely, NSImin simulations show high-latitude cooling and
 180 extratropical and tropical warming that extending up to ~60°N and 40°S. Similar high versus low- latitude contrasts
 181 have been reported in simulations of interglacials characterized by high obliquity and precession, such as Mid-
 182 Holocene (Brierley et al., 2020; Dai et al., 2024) and other interglacials [Yin and Berger, 2012; Herold et al 2012].
 183 These patterns are primarily related to the change in obliquity and precession, and are further amplified by feedback
 184 including high-latitude albedo changes and shifts in the tropical hydrological cycle (Fig. S7 & S8).
 185



186

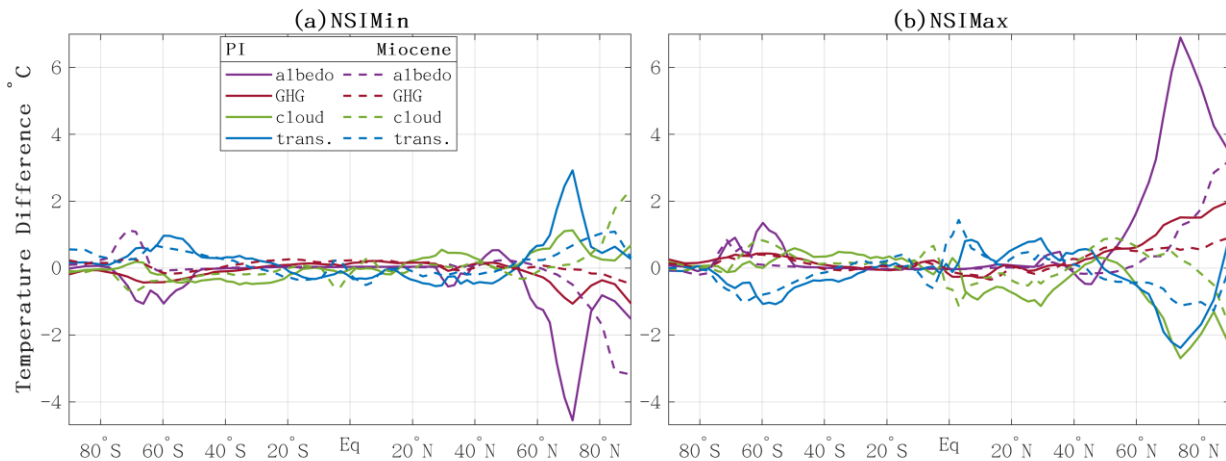
187 **Figure 3. Annual-mean air temperature response (°C).** Upper panel: Anomalies of NSImax and NSImin
 188 simulations relative to the baseline simulation (a, b) and the difference between NSImax and NSImin
 189 (c), all for the PI. Cross marked regions indicate where precipitation increased (red) or decreased (blue) by more
 190 than 0.6 mm/day. Hatching indicates regions where albedo increase (magenta) or decrease (green) by over 5%.

191 Middle panel: Same as upper panel but for the Miocene. Lower panel: Differences between the Miocene and PI
 192 baseline simulations for the NSImax (g) and for the NSImin (h). Blue horizontal and purple vertical hatching regions
 193 indicate where the sign of anomalies is reversed—shifting from negative in PI to positive in Miocene, and vice
 194 versa.

195 **3.2.1 Reduced High-latitude Orbital Response in the Miocene**

196 Compared to PI, the Miocene orbital response is notably weaker at high northern latitudes (Fig. 3). Under PI
 197 conditions, the strongest PINSImax warming (~4.8 °C) occurs over northeast Canada and the Labrador Sea, whereas
 198 the MCONSImax warming is less than half as large (Fig. 3b). Similarly, cooling in the PINSImin simulation reaches
 199 ~4.4 °C over Western Siberia, but only ~1 °C in MCONSImin (Fig. 3a, 3c). The strongest Miocene response —2.8°C
 200 over the Chukchi Sea—remains weaker than its PI counterpart.

201 EBM results show that much of the weaker Miocene temperature responses in NH high-latitudes can be attributed to
 202 smaller changes in surface albedo (Fig. 4). In the Miocene, the albedo contribution is roughly half of that in the PI.
 203 For example, albedo-driven warming reaches ~6 °C in PINSImax but only ~3 °C in MINSImax. Similarly,
 204 MCONSImin shows poleward-shifted and weaker albedo-driven cooling than PINSImin. This reduced albedo
 205 feedback dampens the Miocene temperature responses to orbital forcing, with temperature changes closely matching
 206 the spatial pattern of the Miocene albedo response (Fig. 3). Further analysis (Fig. S7) shows that strong albedo
 207 changes in the PI simulations coincides with ice sheets and sea ice, where ice–albedo feedbacks amplifies the
 208 climate response to orbital forcing. By contrast, the warmer Miocene climate, characterized by widespread
 209 vegetation, limited sea ice, and lower surface albedo, is less sensitive to orbital perturbations.



210
 211 **Figure 4. Zonal mean surface temperature responses to orbital forcing from the EBM decomposition.** Total response is
 212 decomposed into contributions from the surface albedo (albedo), water vapor’s greenhouse (GHG), meridional heat transport
 213 (trans), and cloud effects (cloud).

214 The strong albedo response is further reinforced by water-vapor greenhouse effect but partly offset by cloud
 215 changes. Water-vapor contributions largely follow albedo patterns, reflecting their dependence on surface energy
 216 availability, whereas clouds exert an opposing influence. Further decomposition into shortwave and longwave

217 components reveal that shortwave cloud radiative effects dominate, yielding a generally weaker net negative
218 feedback in the Miocene (Fig. S4).

219 These results are consistent with previous studies suggesting weaker climate sensitivity during warm periods
220 (Reichgelt et al., 2023; De Vleeschouwer et al., 2017; Levy et al., 2019; Naish et al., 2009). For example, proxy
221 reconstruction indicates muted Miocene temperature variability in eastern North America compared to the modern
222 era (Reichgelt et al., 2023). The larger temperature variations in the PI simulation point to enhanced sensitivity to
223 orbital forcing, consistent with the development of pronounced NH glacial-interglacial cycles. In contrast, the
224 Miocene's dampened response implies weakened temperature response to orbital forcing and thus possibly reduced
225 amplitude of orbital-scale climate variability under warmer background conditions.

226 **3.2.2 Enhanced tropical North Africa cooling in the MCONSI_{max}**

227 An exception to the weaker Miocene response is the enhanced tropical North Africa cooling in the MCONSI_{max}
228 simulation (Fig. 3d). Here, annual-mean temperature decreases by 4.4 °C—greater than the 3.8 °C in PINSI_{max}—
229 and the anomaly extends farther north. Seasonal decomposition indicates that this cooling persists even during
230 boreal summer, despite increased insolation (Fig. S1 & S8). It coincides with intensified precipitation, indicating a
231 dominant role of hydrological changes in controlling temperature.

232 These enhanced Miocene cooling effects under MCONSI_{max} are consistent with increased precipitation. EBM
233 diagnostics further reveal a stronger cooling contribution from water-vapor and cloud in Miocene (-0.34 and -
234 1.12°C), in contrast to warming contributions in PI (0.28 and 0.94°C). Additional analysis of moisture flux
235 divergence suggests that more moisture is from the Tethys Sea during the Miocene, feeding precipitation over
236 tropical North Africa (Fig. S9). A wider Tethys Sea provides an efficient moisture source, while a warmer climate
237 accelerates the hydrological cycle (Fig. S8) (Sarr et al., 2022; Huntington, 2006). These findings are in line with
238 proxy evidence for intensified hydrological cycle and increased precipitation under warm climate, such as the “green
239 Sahara” during the mid-Holocene (Hoelzmann et al., 2001; Kutzbach and Liu, 1997; Liu et al., 2024), and support
240 the interpretation that MCONSI_{max} cooling is driven by hydrological intensification. Similar deep-time sensitivity
241 to orbital forcing has been noted in early Cenozoic simulation, which show substantial precipitation responses
242 comparable to monsoon signals (Zhang et al., 2024).

243 **3.2.3 Disrupted Southern Ocean warming in the MCONSI_{min}**

244 In MCONSI_{min} simulation, unexpected warming occurs over the Ross and Weddell Sea despite reduced local
245 annual-mean insolation, in contrast to the cooling simulated in PINSI_{min}. This Miocene response deviates from the
246 near-symmetric responses observed in PI, which broadly follows local insolation changes.

247 This anomalous warming is particularly evident during Austral winter (Fig. S11), disrupting the expected anti-phase
248 signal and generating an out-of-phase response. EBM analysis indicates that the reversed temperature response in
249 MCONSI_{min} (1.1°C warming at 71 °S instead of cooling) is mainly attributed to albedo and water-vapor effects
250 (Fig. 4). During the Miocene, the maximum sea-ice edge lies closer to the pole (~70°S), where significant winter

251 insolation anomalies (Fig. S10) promote positive ice-albedo feedback: reducing sea ice and enhanced ocean-
252 atmosphere heat exchange, and additional atmospheric water vapor (Fig. 3 & S11). In contrast, PI sea ice extends to
253 lower latitudes, where insolation changes were smaller, limiting sensitivity to seasonal orbital forcing (Fig. S11).

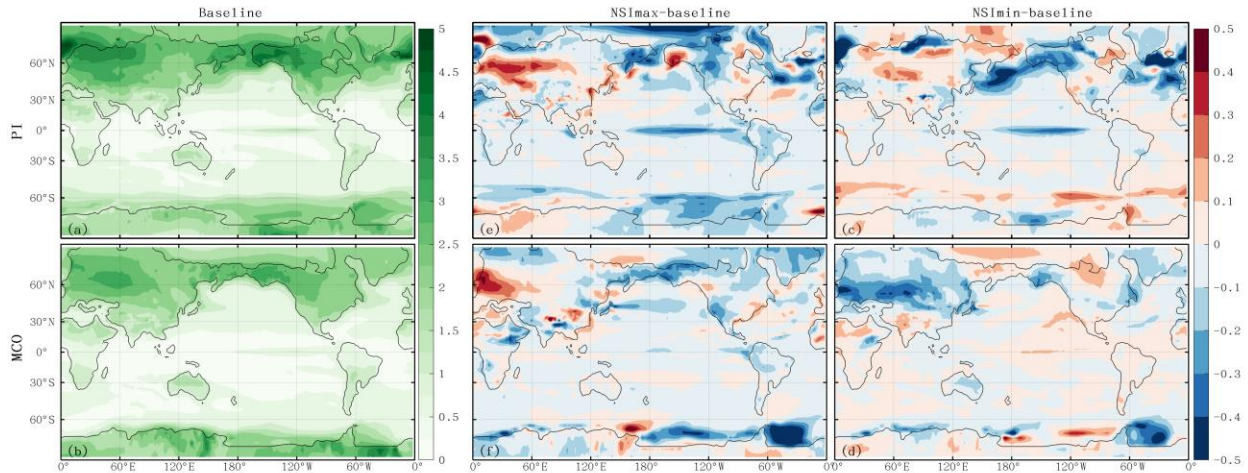
254 These results support geological evidence that ocean-atmosphere-ice sheet interactions amplified Antarctic ice-
255 sheets sensitivity to orbital forcing during Miocene ice-sheet growth (De Vleeschouwer et al., 2017; Levy et al.,
256 2019; Naish et al., 2009). Sediment records further indicate a stronger and more stable climate response as ice sheets
257 and sea ice expanded, compared with warmer periods such as the Early Eocene, when carbon-climate coupling
258 dominated (De Vleeschouwer et al., 2017; Levy et al., 2019; Naish et al., 2009; Reichgelt et al., 2023)(Setty et al.,
259 2023). Overall, these findings underscore strong background-state control on Southern Ocean sea-ice feedbacks
260 (Bloch - Johnson et al., 2021).

261 **3.3 Spatially diverse Miocene responses to orbital forcing and weakened internal temperature variability**

262 Beyond differences in magnitude, the spatial extent of warming and cooling response also differs between the PI and
263 Miocene simulation. Under PI conditions, high-latitude temperature responses are largely symmetric between
264 NSImax and NSImin. In contrast, the Miocene simulations show warming in both MCONSImin and MCONSImax
265 over Siberia and Alaska, resulting in distinct regional responses across 60-70°N spanning Eurasia, Alaska and North
266 America continent (Fig. 3e, blue line). Similarly, the Weddell Sea and Ross Sea exhibit overall warming in both
267 Miocene orbital simulations, deviating from the symmetric PI behavior (Fig. 3 & S11). These deviations suggest a
268 less symmetric and less predictable Miocene response, likely consistent with proxy evidence for dominance of
269 longer-period orbital variability (e.g. the 400-kyr) rather than 40 kyr and 100 kyr cycle characteristic of the
270 Pleistocene [Holbourn et al., 2007; Tian et al., 2013; Westerhold et al., 2020; Liu et al., 2024]. This also implies that
271 simple NSImax minus NSImin, without examining spatial patterns in detail, can obscure nonlinear responses—
272 particularly under warmer background conditions.

273 In addition to mean changes, internal temperature variability provides insight into climate stability (Harzhauser et
274 al., 2011). We therefore examine de-seasonalised variability (standard deviation) over key high-latitude regions of
275 active glacial dynamics. Mid-latitude Eurasia and North America exhibit higher variability in the PI simulation,
276 which is further amplified in both PINSImin and PINSImax, reflecting enhanced ice-albedo interactions and land-
277 atmosphere coupling. By contrast, Miocene variability is lower and further reduced in MCONSImin (Fig. 5),
278 suggesting a more stable high-latitude climate with dampened feedbacks under warmer conditions. Reduced eastern
279 Pacific variability in the Miocene likely reflects enhanced inter-basin exchange through an open Panama Seaway,
280 which buffers regional responses. The stronger PI variability supports pronounced NH glacial-interglacial cycles,
281 whereas the dampened Miocene response suggests weaker orbital pacing.

282



283

284 **Figure 5. Standard deviation of deseasonalized temperature, and its responses to orbital forcing.**

285 **4 Conclusions and Implications**

286 The Miocene, particularly the interval following the Miocene Climatic Optimum (MCO), shows strong orbital
 287 pacing in geological records despite warm boundary conditions, limited Northern Hemisphere ice, and reduced
 288 meridional temperature gradients. However, the mechanisms linking orbital forcing to climate variability during this
 289 warm epoch are not well understood. By conducting parallel orbital sensitivity experiments under mid-Miocene and
 290 pre-industrial (PI) conditions, we evaluate how background climate state modulates the expression of orbital-driven
 291 temperature change.

292 In general, both temperature exhibit broadly anti-phased temperature responses between maximum and minimum
 293 boreal summer insolation, each characterized by a meridional high-to-low latitude dipole. However, the Miocene
 294 response is $\sim 1^\circ\text{C}$ weaker, with regionally dependent contrasts and reduced symmetry between two orbital cases.
 295 Three key differences emerge: (1) reduced Northern Hemisphere continental sensitivity in the Miocene, reflecting
 296 weaker surface-albedo, water-vapor, and cloud radiative effects in a warmer, low-ice, vegetation-modified climate—
 297 consistent with proxy evidence for diminished high-latitude climate sensitivity after the MCO; (2) stronger
 298 hydrological cooling in North Tropical Africa in MCONSI_{max}, driven by enhanced precipitation, cloud, and
 299 moisture-feedbacks within an intensified Miocene hydrological cycle supported by a wider Tethys Sea —indicating
 300 amplified hydrological sensitivity to orbital forcing in warm climates; and (3) a reversed Southern Ocean warming
 301 in MCONSI_{min} under lower insolation, where poleward-restricted Miocene sea ice allows winter insolation
 302 anomalies to trigger positive ice-albedo feedbacks, matching proxy evidence for heightened Antarctic obliquity
 303 sensitivity.

304 These differences highlight that the strength and pattern of orbital impact depend strongly on background climate
 305 state. The Miocene’s weaker seasonal amplitude and reduced internal variability imply diminished orbital pacing
 306 relative to the PI climate, consistent with dominant 400-kyr eccentricity variability in Miocene proxy records. This

307 has two key implications: first, Miocene proxy reconstructions may overestimate annual mean temperatures if
308 modern seasonal analogues are applied, underscoring the need for context-specific seasonality corrections; and
309 second, the stronger and more symmetric PI response reflects the emergence of high-latitude cryosphere feedbacks
310 central to Quaternary glacial–interglacial cycles.

311

312 **Acknowledgments**

313 The authors are grateful to the two anonymous referees for their valuable comments that substantially improved the
314 manuscript, as well as the Editor, Ran Feng, for managing the review process. This study was supported by the
315 National Key R&D program of China (2023YFF0803902) and (2023YFF0803904). We appreciate the technical
316 support of the National Large Scientific and Technological Infrastructure, *Earth System Numerical Simulation*
317 *Facility* (<https://estr.cn/31134.02.EL>).

318

319 **Open Research**

320 Model output data from this study are available at Zhang (2025).

321

322 **Author contributions**

323 Conceptualization & Study Design: YZ;

324 Methodology & Simulations: YZ, JW, with support from WZ;

325 Formal Analysis & Investigation: YZ, with guidance from YQ, A. de B., ZS, LZ;

326 Data Curation: ZL, ND;

327 Writing – Original Draft: YZ;

328 Writing – Review & Editing: All authors.

329

330 **Competing interests**

331 Some authors are members of the editorial board of journal *Climate of the Past*.

332

333 **References**

334 Anttila, E. S. C., Macdonald, F. A., Szymanowski, D., Schoene, B., Kylander-Clark, A., Danhof, C., and Jones, D. S.:
335 Timing and tempo of organic carbon burial in the Monterey Formation of the Santa Barbara Basin and relationships

336 with Miocene climate, *Earth and Planetary Science Letters*, 620, 10.1016/j.epsl.2023.118343, 2023.

337 Battisti, D. S., Ding, Q., and Roe, G. H.: Coherent pan-Asian climatic and isotopic response to orbital forcing of
338 tropical insolation, *Journal of Geophysical Research: Atmospheres*, 119, 10.1002/2014jd021960, 2014.

339 Berger: Long-Term Variations of Daily Insolation and Quaternary Climatic Changes %J *Journal of Atmospheric*
340 *Sciences*, 35, 2362-2367, [https://doi.org/10.1175/1520-0469\(1978\)035<2362:LTVODI>2.0.CO;2](https://doi.org/10.1175/1520-0469(1978)035<2362:LTVODI>2.0.CO;2), 1978.

341 Berger, Yin, Q., and Wu, Z.: Length of astronomical seasons, total and average insolation over seasons, *Quaternary*
342 *Science Reviews*, 334, 108620, <https://doi.org/10.1016/j.quascirev.2024.108620>, 2024.

343 Bloch-Johnson, J., Rugenstein, M., Stolpe, M. B., Rohrschneider, T., Zheng, Y., and Gregory, J. M.: Climate Sensitivity
344 Increases Under Higher CO2 Levels Due to Feedback Temperature Dependence, *Geophysical Research Letters*, 48,
345 10.1029/2020gl089074, 2021.

346 Bosmans, J. H. C., Erb, M. P., Dolan, A. M., Drijfhout, S. S., Tuenter, E., Hilgen, F. J., Edge, D., Pope, J. O., and
347 Lourens, L. J.: Response of the Asian summer monsoons to idealized precession and obliquity forcing in a set of
348 GCMs, *Quaternary Science Reviews*, 188, 121-135, 10.1016/j.quascirev.2018.03.025, 2018.

349 Bova, S., Rosenthal, Y., Liu, Z., Godad, S. P., and Yan, M.: Seasonal origin of the thermal maxima at the Holocene
350 and the last interglacial, *Nature*, 589, 548-553, 10.1038/s41586-020-03155-x, 2021.

351 Brierley, C. M., Zhao, A., Harrison, S. P., Braconnot, P., Williams, C. J. R., Thornalley, D. J. R., Shi, X., Peterschmitt,
352 J.-Y., Ohgaito, R., Kaufman, D. S., Kageyama, M., Hargreaves, J. C., Erb, M. P., Emile-Geay, J., D'Agostino, R.,
353 Chandan, D., Carré, M., Bartlein, P. J., Zheng, W., Zhang, Z., Zhang, Q., Yang, H., Volodin, E. M., Tomas, R. A.,
354 Routson, C., Peltier, W. R., Otto-Bliesner, B., Morozova, P. A., McKay, N. P., Lohmann, G., Legrande, A. N., Guo, C.,
355 Cao, J., Brady, E., Annan, J. D., and Abe-Ouchi, A.: Large-scale features and evaluation of the PMIP4-CMIP6
356 midHolocene simulations, *Climate of the Past*, 16, 1847-1872, 10.5194/cp-16-1847-2020, 2020.

357 Burls, N. J., Bradshaw, C. D., De Boer, A. M., Herold, N., Huber, M., Pound, M., Donnadieu, Y., Farnsworth, A.,
358 Frigola, A., Gasson, E., von der Heydt, A. S., Hutchinson, D. K., Knorr, G., Lawrence, K. T., Lear, C. H., Li, X.,
359 Lohmann, G., Lunt, D. J., Marzocchi, A., Prange, M., Riihimaki, C. A., Sarr, A. C., Siler, N., and Zhang, Z.: Simulating
360 Miocene Warmth: Insights From an Opportunistic Multi-Model Ensemble (MioMIP1), *Paleoceanography and*
361 *Paleoclimatology*, 36, 10.1029/2020pa004054, 2021.

362 Dai, G., Zhang, Z., Otterå, O. H., Langebroek, P. M., Yan, Q., Zhang, R., and Zhu, Z.: Winter Insolation Modulates
363 Boreal Tropical Monsoonal Temperatures in the Late Pleistocene, *Journal of Geophysical Research: Atmospheres*,
364 129, 10.1029/2023jd040577, 2024.

365 De Vleeschouwer, D., Vahlenkamp, M., Crucifix, M., and Pälike, H.: Alternating Southern and Northern Hemisphere
366 climate response to astronomical forcing during the past 35 m.y, *Geology*, 45, 375-378, 10.1130/g38663.1, 2017.

367 Harzhauser, M., Piller, W. E., Müllegger, S., Grunert, P., and Micheels, A.: Changing seasonality patterns in Central
368 Europe from Miocene Climate Optimum to Miocene Climate Transition deduced from the *Crassostrea* isotope archive,
369 *Global and Planetary Change*, 76, 77-84, 10.1016/j.gloplacha.2010.12.003, 2011.

370 Hays, J. D., Imbrie, J., and Shackleton, N. J.: Variations in the Earth's Orbit: Pacemaker of the Ice Ages, 194, 1121-
371 1132, doi:10.1126/science.194.4270.1121, 1976.

372 Heinemann, M., Jungclaus, J. H., and Marotzke, J.: Warm Paleocene/Eocene climate as simulated in ECHAM5/MPI-
373 OM, *Clim. Past*, 5, 785-802, 10.5194/cp-5-785-2009, 2009.

374 Herold, N., Yin, Q. Z., Karami, M. P., and Berger, A.: Modelling the climatic diversity of the warm interglacials,
375 *Quaternary Science Reviews*, 56, 126-141, <https://doi.org/10.1016/j.quascirev.2012.08.020>, 2012.

376 Hoelzmann, P., Keding, B., Berke, H., Kröpelin, S., and Kruse, H.-J.: Environmental change and archaeology: lake
377 evolution and human occupation in the Eastern Sahara during the Holocene, *Palaeogeography, Palaeoclimatology,*
378 *Palaeoecology*, 169, 193-217, [https://doi.org/10.1016/S0031-0182\(01\)00211-5](https://doi.org/10.1016/S0031-0182(01)00211-5), 2001.

379 Holbourn, A., Kuhnt, W., Clemens, S., Prell, W., and Andersen, N.: Middle to late Miocene stepwise climate cooling:
380 Evidence from a high-resolution deep water isotope curve spanning 8 million years, *Paleoceanography*, 28, 688-699,
381 10.1002/2013pa002538, 2013.

382 Holbourn, A., Kuhnt, W., Schulz, M., Flores, J.-A., and Andersen, N.: Orbitally-paced climate evolution during the
383 middle Miocene “Monterey” carbon-isotope excursion, *Earth and Planetary Science Letters*, 261, 534-550,
384 10.1016/j.epsl.2007.07.026, 2007.

385 Holbourn, A., Kuhnt, W., Clemens, S. C., Kochhann, K. G. D., Johnck, J., Lubbers, J., and Andersen, N.: Late Miocene
386 climate cooling and intensification of southeast Asian winter monsoon, *Nat Commun*, 9, 1584, 10.1038/s41467-018-
387 03950-1, 2018.

388 Huntington, T. G.: Evidence for intensification of the global water cycle: Review and synthesis, *Journal of Hydrology*,
389 319, 83-95, <https://doi.org/10.1016/j.jhydrol.2005.07.003>, 2006.

390 Kemp, A. E. S., Grigorov, I., Pearce, R. B., and Naveira Garabato, A. C.: Migration of the Antarctic Polar Front through
391 the mid-Pleistocene transition: evidence and climatic implications, *Quaternary Science Reviews*, 29, 1993-2009,
392 <https://doi.org/10.1016/j.quascirev.2010.04.027>, 2010.

393 Kutzbach, J. E. and Liu, Z.: Response of the African monsoon to orbital forcing and ocean feedbacks in the middle
394 holocene, 278, *Medium: X*; Size: pp. 440-443, 10.1126/science.278.5337.440, 1997.

395 Laepple and Lohmann, G.: Seasonal cycle as template for climate variability on astronomical timescales,
396 *Paleoceanography*, 24, 10.1029/2008pa001674, 2009.

397 Laepple, Shakun, J., He, F., and Marcott, S.: Concerns of assuming linearity in the reconstruction of thermal maxima,
398 *Nature*, 607, E12-E14, 10.1038/s41586-022-04831-w, 2022.

399 Laskar, J. A. F. M. G. H. M.: La2010: a new orbital solution for the long-term motion of the Earth, *Astronomy &*
400 *Astrophysics*, 532, A89 (2011), 10.1051/0004-6361/201116836, 2010.

401 Levy, R. H., Meyers, S. R., Naish, T. R., Golledge, N. R., McKay, R. M., Crampton, J. S., DeConto, R. M., De Santis,
402 L., Florindo, F., Gasson, E. G. W., Harwood, D. M., Luyendyk, B. P., Powell, R. D., Clowes, C., and Kulhanek, D. K.:
403 Antarctic ice-sheet sensitivity to obliquity forcing enhanced through ocean connections, *Nature Geoscience*, 12, 132-
404 137, 10.1038/s41561-018-0284-4, 2019.

405 Li, L. Y., Yongqiang, Tang, Y., Lin, P., Xie, J., Song, M., Dong, L., Zhou, T., Liu, L., Wang, L., Pu, Y., Chen, X., Chen,
406 L., Xie, Z., Liu, H., Zhang, L., Huang, X., Feng, T., Zheng, W., Xia, K., Liu, H., Liu, J., Wang, Y., Wang, L., Jia, B.,
407 Xie, F., Wang, B., Zhao, S., Yu, Z., Zhao, B., and Wei, J.: The Flexible Global Ocean-Atmosphere-Land System Model
408 Grid-Point Version 3 (FGOALS-g3): Description and Evaluation, *Journal of Advances in Modeling Earth Systems*,
409 12, 10.1029/2019ms002012, 2020.

410 Lin, P., Zhao, B., Wei, J., Liu, H., Zhang, W., Chen, X., Jiang, J., Ding, M., Man, W., Jiang, J., Zhang, X., Ding, Y.,
411 Bai, W., Jin, C., Yu, Z., Li, Y., Zheng, W., and Zhou, T.: The Super-large Ensemble Experiments of CAS FGOALS-
412 g3, *Advances in Atmospheric Sciences*, 39, 1746-1765, 10.1007/s00376-022-1439-1, 2022.

413 Liu, F., Du, J., Huang, E., Ma, W., Ma, X., Lourens, L. J., and Tian, J.: Accelerated marine carbon cycling forced by
414 tectonic degassing over the Miocene Climate Optimum, *Sci Bull (Beijing)*, 69, 823-832, 10.1016/j.scib.2023.12.052,
415 2024.

416 Lunt, D. J., Haywood, A. M., Schmidt, G. A., Salzmann, U., Valdes, P. J., Dowsett, H. J., and Loftson, C. A.: On the
417 causes of mid-Pliocene warmth and polar amplification, *Earth and Planetary Science Letters*, 321-322, 128-138,
418 10.1016/j.epsl.2011.12.042, 2012.

419 Marsicek, J., Shuman, B. N., Bartlein, P. J., Shafer, S. L., and Brewer, S.: Reconciling divergent trends and millennial
420 variations in Holocene temperatures, *Nature*, 554, 92-96, 10.1038/nature25464, 2018.

421 Milanković, M. M.: Canon of insolation and the ice-age problem. Beograd, Koninglich Serbische Akademie. 484 pp.
422 [English translation by Israel Porgram for Scientific Translation and published by the U.S. Dept. of Commerce and

423 national Science Foundation.], 1941.

424 Naish, T., Powell, R., Levy, R., Wilson, G., Scherer, R., Talarico, F., Krissek, L., Niessen, F., Pompilio, M., Wilson,
425 T., Carter, L., DeConto, R., Huybers, P., McKay, R., Pollard, D., Ross, J., Winter, D., Barrett, P., Browne, G., Cody,
426 R., Cowan, E., Crampton, J., Dunbar, G., Dunbar, N., Florindo, F., Gebhardt, C., Graham, I., Hannah, M., Hansaraj,
427 D., Harwood, D., Helling, D., Henrys, S., Hinnov, L., Kuhn, G., Kyle, P., Laufer, A., Maffioli, P., Magens, D.,
428 Mandernack, K., McIntosh, W., Millan, C., Morin, R., Ohneiser, C., Paulsen, T., Persico, D., Raine, I., Reed, J.,
429 Riesselman, C., Sagnotti, L., Schmitt, D., Sjunneskog, C., Strong, P., Taviani, M., Vogel, S., Wilch, T., and Williams,
430 T.: Obliquity-paced Pliocene West Antarctic ice sheet oscillations, *Nature*, 458, 322-328, 10.1038/nature07867, 2009.

431 Reichgelt, T., Baumgartner, A., Feng, R., and Willard, D. A.: Poleward amplification, seasonal rainfall and forest
432 heterogeneity in the Miocene of the eastern USA, *Global and Planetary Change*, 222,
433 10.1016/j.gloplacha.2023.104073, 2023.

434 Sarr, A.-C., Donnadieu, Y., Bolton, C. T., Ladant, J.-B., Licht, A., Fluteau, F., Laugié, M., Tardif, D., and Dupont-
435 Nivet, G.: Neogene South Asian monsoon rainfall and wind histories diverged due to topographic effects, *Nature*
436 *Geoscience*, 15, 314-319, 10.1038/s41561-022-00919-0, 2022.

437 Setty, S., Cramwinckel, M. J., van Nes, E. H., van de Leemput, I. A., Dijkstra, H. A., Lourens, L. J., Scheffer, M., and
438 Sluijs, A.: Loss of Earth system resilience during early Eocene transient global warming events, *Science Advances*, 9,
439 eade5466, 10.1126/sciadv.ade5466, 2023.

440 Steinhorsdottir, M., Coxall, H. K., de Boer, A. M., Huber, M., Barbolini, N., Bradshaw, C. D., Burls, N. J., Feakins,
441 S. J., Gasson, E., Henderiks, J., Holbourn, A. E., Kiel, S., Kohn, M. J., Knorr, G., Kürschner, W. M., Lear, C. H.,
442 Liebrand, D., Lunt, D. J., Mörs, T., Pearson, P. N., Pound, M. J., Stoll, H., and Strömberg, C. A. E.: The Miocene: The
443 Future of the Past, *Paleoceanography and Paleoclimatology*, 36, 10.1029/2020pa004037, 2021.

444 Tardif, D., Toumoulin, A., Fluteau, F., Donnadieu, Y., Le Hir, G., Barbolini, N., Licht, A., Ladant, J.-B., Sepulchre, P.,
445 Viovy, N., Hoorn, C., and Dupont-Nivet, G.: Orbital variations as a major driver of climate and biome distribution
446 during the greenhouse to icehouse transition, *Science Advances*, 7, eabh2819, 10.1126/sciadv.abh2819, 2021.

447 Tian, J., Yang, M., Lyle, M. W., Wilkens, R., and Shackford, J. K.: Obliquity and long eccentricity pacing of the Middle
448 Miocene climate transition, *Geochemistry, Geophysics, Geosystems*, 14, 1740-1755, 10.1002/ggge.20108, 2013.

449 Utescher, T., Ivanov, D., Harzhauser, M., Bozukov, V., Ashraf, A. R., Rolf, C., Urbat, M., and Mosbrugger, V.: Cyclic
450 climate and vegetation change in the late Miocene of Western Bulgaria, *Palaeogeography, Palaeoclimatology,*
451 *Palaeoecology*, 272, 99-114, 10.1016/j.palaeo.2008.11.014, 2009.

452 van Peer, T. E., Liebrand, D., Taylor, V. E., Brzelinski, S., Wolf, I., Bornemann, A., Friedrich, O., Bohaty, S. M., Xuan,
453 C., Lippert, P. C., and Wilson, P. A.: Eccentricity pacing and rapid termination of the early Antarctic ice ages, *Nat*
454 *Commun*, 15, 10600, 10.1038/s41467-024-54186-1, 2024.

455 Wang, Y., Yu, Z., Lin, P., Liu, H., Jin, J., Li, L., Tang, Y., Dong, L., Chen, K., Li, Y., Yang, Q., Ding, M., Meng, Y.,
456 Zhao, B., Wei, J., Ma, J., and Sun, Z.: FGOALS-g3 Model Datasets for CMIP6 Flux-Anomaly-Forced Model
457 Intercomparison Project, *Advances in Atmospheric Sciences*, 37, 1093-1101, 10.1007/s00376-020-2045-8, 2020.

458 Wei, J., Liu, H., Zhao, Y., Lin, P., Yu, Z., Li, L., Xie, J., and Duan, A.: Simulation of the climate and ocean circulations
459 in the Middle Miocene Climate Optimum by a coupled model FGOALS-g3, *Palaeogeography, Palaeoclimatology,*
460 *Palaeoecology*, 617, 10.1016/j.palaeo.2023.111509, 2023.

461 Westerhold, T., Marwan, N., Drury, A. J., Liebrand, D., Agnini, C., Anagnostou, E., Barnett, J. S. K., Bohaty, S. M.,
462 De Vleeschouwer, D., Florindo, F., Frederichs, T., Hodell, D. A., Holbourn, A. E., Kroon, D., Lauretano, V., Littler,
463 K., Lourens, L. J., Lyle, M., Pälike, H., Röhl, U., Tian, J., Wilkens, R. H., Wilson, P. A., and Zachos, J. C.: An
464 astronomically dated record of Earth's climate and its predictability over the last 66 million years, 369, 1383-1387,
465 doi:10.1126/science.aba6853, 2020.

466 Yin, Q., and Berger, A.: Individual contribution of insolation and CO₂ to the interglacial climates of the past
467 800,000 years, *Climate Dynamics*, 38, 709-724, 10.1007/s00382-011-1013-5, 2012.

- 468 Yin, Q.: Insolation-induced mid-Brunhes transition in Southern Ocean ventilation and deep-ocean temperature, *Nature*,
469 494, 222-225, 10.1038/nature11790, 2013.
- 470 Zhang, Z., Zhang, Z., Zhang, Z., Tan, N., He, Z., Huang, C., and Guo, Z.: Resolving Cenozoic climate pattern debate
471 in East Asia: Insights from orbital-scale oscillations, *Global and Planetary Change*, 232, 104346,
472 <https://doi.org/10.1016/j.gloplacha.2023.104346>, 2024.
- 473 Zheng, W., Yu, Y., Luan, Y., Zhao, S., He, B., Dong, L., Song, M., Lin, P., and Liu, H.: CAS-FGOALS Datasets for
474 the Two Interglacial Epochs of the Holocene and the Last Interglacial in PMIP4, *Advances in Atmospheric Sciences*,
475 37, 1034-1044, 10.1007/s00376-020-9290-8, 2020.